American Mineralogist, Volume 97, pages 1103–1115, 2012

Characterization of fluor-chlorapatites by electron probe microanalysis with a focus on time-dependent intensity variation of halogens

Beth Goldoff,[1,*] James D. Webster,[1] and Daniel E. Harlov[2]

[1]Department of Earth and Planetary Sciences, American Museum of Natural History, Central Park West at 79th Street, New York, New York 10024-5192, U.S.A.
[2]Section 3.3, GeoForschungsZentrum, Telegrafenberg, D-14473 Potsdam, Germany

Abstract

Prior research has shown that fluorine and chlorine X-ray count rates vary with exposure to the electron beam during electron probe microanalysis (EPMA) of apatite. Stormer et al. (1993) and Stormer and Pierson (1993) demonstrate that the EPMA-operating conditions affect the halogen intensities in F-rich natural Durango and Wilberforce apatites and in a Cl-rich apatite. Following these studies, we investigated the effects of operating conditions on time-dependent X-ray intensity variations of F and Cl in a broad range of anhydrous fluor-chlorapatites. We tested 7, 10, and 15 kV accelerating voltages; 4, 10, and 15 nA beam currents; 2, 5, and 10 μm diameter fixed spot sizes; and the influence of 2 distinct crystal orientations under the electron beam. We find that the halogen X-ray intensity variations fluctuate strongly with operating conditions and the bulk F and Cl contents of apatite.

We determined the optimal EPMA operating conditions for these anhydrous fluor-chlorapatites to be: 10 kV accelerating voltage, 4 nA beam current (measured at the Faraday cup), 10 μm diameter fixed spot, and the apatite crystals oriented with their *c*-axes perpendicular to the incident electron beam. This EPMA technique was tested on a suite of 19 synthetic anhydrous apatites that covers the fluorapatite-chlorapatite solid-solution series. The results of these analyses are highly accurate; the F and Cl EPMA data agree extremely well with wet-chemical analyses and have an R^2 value >0.99.

Keywords: Fluorapatite, chlorapatite, fluor-chlorapatite, EPMA measurement, fluorine, chlorine, Durango fluorapatite

Introduction

Apatite [$Ca_5(PO_4)_3(F,Cl,OH)$] is a common accessory mineral found in a large variety of sedimentary, metamorphic, and igneous rocks. Of the three end-members, fluorapatite [$Ca_5(PO_4)_3F$] is the most abundant in nature followed, to a significantly lesser extent, by chlorapatite [$Ca_5(PO_4)_3Cl$] and hydroxylapatite [$Ca_5(PO_4)_3OH$], though F-rich apatites commonly contain minor chlorapatite and hydroxlapatite components. Fluorine-rich apatite serves as one of the principle reservoirs for phosphorus in the Earth's crust. The low solubility of apatite in most melts and fluids allows it to persist in many igneous and metamorphic environments (Piccoli and Candela 2002). Though F-rich apatite is usually an accessory mineral, its composition reflects the overall geochemistry and history of the geologic environments in which it has grown and potentially re-equilibrated (Patiño Douce and Roden 2006; Boyce and Hervig 2008). Fluorine-rich apatite also is an important indicator mineral for investigations based on trace-element geochemistry (Campbell and Henderson 1997; Pan and Fleet 2002; Harlov and Förster 2003; Klemme and Dalpé 2003).

Fluorine and chlorine serve as important volatile components of magmatic and metamorphic systems, including those in extraterrestrial environments, and their concentrations in the melts and fluids within which F- or Cl-enriched apatite has equilibrated can be directly determined using Nernstian partition coefficients as a function of pressure, temperature, and composition (Piccoli and Candela 2002; Harlov and Förster 2002; Mathez and Webster 2005; Webster et al. 2009; Hansen and Harlov 2007; Boyce et al. 2010; Patiño Douce et al. 2011; McCubbin et al. 2011; Konzett et al. 2012). In addition, apatite is used to estimate magmatic and hydrothermal concentrations of sulfate and carbonate ions in fluid media (Streck and Dilles 1998; Fleet et al. 2004; see summary in Parat et al. 2011) and for fission-track dating (Paul and Fitzgerald 1992; Gleadow et al. 2002).

Apatite occurs as sub-equant, small acicular, and elongated hexagonal crystals in rocks, and may only be tens of micrometers in length. Natural apatite crystals may also be chemically zoned (Piccoli and Candela 2002; Boyce and Hervig 2008). These textural characteristics often make accurate and precise, high-spatial resolution EPMA measurement of the concentrations of F and Cl in apatite problematic. Indeed, a review of the literature reveals that many analyses of apatite report F concentrations that exceed the maximum F concentrations of 3.76 wt% possible in stoichiometric fluorapatite (Pyle et al. 2002 and references therein).

Several sources of EPMA error have been identified by Stormer et al. (1993) who demonstrate that the F, Cl, Ca, and P

* E-mail: bgoldoff@amnh.org

0003-004X/12/0007–1103$05.00/DOI: http://dx.doi.org/10.2138/am.2012.3812

Table 1. EPMA operating conditions tested for apatite (this study, Stormer and Pierson 1993, and Stormer et al. 1993)

Spot size (μm)	Current (nA)	Accelerating potential (kV)	Apatite analyzed	Apatite crystal orientation	Study
1	15	15	Durango fluorapatite	*c*-axis oriented parallel to e-beam	Stormer et al. (1993)
2	15	7	Durango fluorapatite	*c*-axis oriented parallel to e-beam	Stormer et al. (1993)
2	15	10	Durango fluorapatite	*c*-axis oriented parallel to e-beam	Stormer et al. (1993)
2	15	15	Durango fluorapatite	*c*-axis oriented perpendicular to e-beam	Stormer et al. (1993)
2	15	15	Durango fluorapatite	*c*-axis oriented parallel to e-beam	Stormer et al. (1993)
3	15	15	Durango fluorapatite	*c*-axis oriented perpendicular to e-beam	Stormer et al. (1993)
3	15	15	Durango fluorapatite	*c*-axis oriented parallel to e-beam	Stormer et al. (1993)
5	15	15	Durango fluorapatite	*c*-axis oriented parallel to e-beam	Stormer et al. (1993)
5	15	15	Chlorapatite*	*c*-axis oriented nearly parallel to e-beam	Stormer et al. (1993)
5	15	15	Chlorapatite*	*c*-axis oriented nearly perpendicular to e-beam	Stormer et al. (1993)
10	15	15	Durango fluorapatite	*c*-axis oriented parallel to e-beam	Stormer et al. (1993)
10	4	7	5 synthetic fluor-chlorapatites	*c*-axis oriented perpendicular to e-beam	This study
10	4	7	5 synthetic fluor-chlorapatites	*c*-axis oriented parallel to e-beam	This study
2	4	10	5 synthetic fluor-chlorapatites	*c*-axis oriented perpendicular to e-beam	This study
2	4	10	5 synthetic fluor-chlorapatites	*c*-axis oriented parallel to e-beam	This study
5	4	10	5 synthetic fluor-chlorapatites	*c*-axis oriented perpendicular to e-beam	This study
5	4	10	5 synthetic fluor-chlorapatites	*c*-axis oriented parallel to e-beam	This study
10	4	10	5 synthetic fluor-chlorapatites	*c*-axis oriented perpendicular to e-beam	This study
10	4	10	5 synthetic fluor-chlorapatites	*c*-axis oriented parallel to e-beam	This study
10	10	10	5 synthetic fluor-chlorapatites	*c*-axis oriented perpendicular to e-beam	This study
10	10	10	5 synthetic fluor-chlorapatites	*c*-axis oriented parallel to e-beam	This study
10	15	10	5 synthetic fluor-chlorapatites	*c*-axis oriented perpendicular to e-beam	This study
10	15	10	5 synthetic fluor-chlorapatites	*c*-axis oriented parallel to e-beam	This study
2	4	15	5 synthetic fluor-chlorapatites	*c*-axis oriented perpendicular to e-beam	This study
2	4	15	5 synthetic fluor-chlorapatites	*c*-axis oriented parallel to e-beam	This study
5	4	15	5 synthetic fluor-chlorapatites	*c*-axis oriented perpendicular to e-beam	This study
5	4	15	5 synthetic fluor-chlorapatites	*c*-axis oriented parallel to e-beam	This study
10	4	15	5 synthetic fluor-chlorapatites	*c*-axis oriented perpendicular to e-beam	This study
10	4	15	5 synthetic fluor-chlorapatites	*c*-axis oriented parallel to e-beam	This study
10	15	15	5 synthetic fluor-chlorapatites	*c*-axis oriented perpendicular to e-beam	This study
10	15	15	5 synthetic fluor-chlorapatites	*c*-axis oriented parallel to e-beam	This study
5	10	15	Durango fluorapatite	*c*-axis oriented perpendicular to e-beam	Stormer and Pierson (1993)
5	10	15	Durango fluorapatite	*c*-axis oriented 44° from e-beam	Stormer and Pierson (1993)
5	10	15	Durango fluorapatite	*c*-axis oriented 67° from e-beam	Stormer and Pierson (1993)
5	10	15	Durango fluorapatite	*c*-axis oriented parallel to e-beam	Stormer and Pierson (1993)
5	10	15	Wilberforce apatite	4 unknown orientations	Stormer and Pierson (1993)

* Chlorapatite contains 2.9 wt% Cl and 0.8 wt% F, from Balme, Norway.

*K*α X-ray counts from the Durango F-rich apatite vary with the operating conditions and with analytical time (Table 1). Importantly, they showed that X-ray emission from apatite under an electron beam is strongly anisotropic. They observed variable fluctuations in halogen X-ray intensities with progressive exposure to the electron beam and noted that the *K*α X-ray intensities of Ca and P vary inversely with that of F over time.

Stormer et al. (1993) investigated the behavior of halogens in the Durango apatite, which contains 3.5 wt% F and 0.4 wt% Cl and in an apatite that bears 2.9 wt% Cl and 0.8 wt% F. Stormer and Pierson (1993) studied F in the Durango apatite and Wilberforce apatite, which contains 3.8 wt% F. These studies were limited to three apatite compositions, two of which are highly fluorine-enriched, and hence, it is important to examine the response of F and Cl to EPMA for a geologically relevant, larger range of apatite compositions. To follow upon and extend this prior research, we have tested the effects of EPMA operating conditions on the time-dependent X-ray intensity (TDI) variation of halogens in a broad spectrum of synthetic anhydrous apatites ranging from fluorapatite to chlorapatite (Tables 1 and 2). From the test results we have determined an optimal set of EPMA operating conditions to analyze this apatite suite. We compare the results produced by this optimized analytical protocol (Table 3) with the associated wet-chemical analyses (Table 4), and demonstrate very close agreement in halogen contents between the two methods.

Table 2. Effect of accelerating potential on emitted X-ray intensity from fluor-chlorapatite*

	7 kV	10 kV	15 kV
F	12	12	10
Cl	40	96	200
Ca	151	471	1246
P	364	765	1437

* Data are counts per second per nanoamp of X-rays emitted from apatite APS-35 (1.57 wt% F, 3.66 wt% Cl) during first 10 s of electron probe microanalysis conducted with a 7, 10, or 15 kV accelerating potential, 4 nA beam current, 10 μm diameter spot, and the apatite crystal oriented with its *c*-axis perpendicular to the electron beam; averages of 2–4 analyses each.

Analytical methods

Samples analyzed

The X-ray intensity data were collected on 5 anhydrous apatite samples APS-21, APS-27, APS-35, APS-16, and APS-26 that span the fluor-chlorapatite solid-solution series (Table 4). These fluor-chlorapatites were synthesized at 1220–1375 °C from $Ca_3(PO_4)_2$ dissolved in a molten CaF_2-$CaCl_2$ flux (Schettler et al. 2011). The compositions were subsequently determined using a recently developed semi-microanalytical wet-chemical technique that involves HNO_3 digestion and ion exchange chromatography for F^- and Cl^- determination and ICP-AES for Ca and P determination (Schettler et al. 2011). The analytical results were confirmed by charge balance; (Ca/P), [Ca/(F+Cl)], and [P/(F+Cl)] ratios; and the total cation sums. The apatites also were characterized structurally by powder and single-crystal X-ray diffraction (XRD) analysis. XRD analysis and high-contrast backscattered electron (BSE) imaging of this series indicate that these fluorapatite and chlorapatite samples form a continuous solid-solution series across the join with no indication of a miscibility gap at the temperatures of synthesis (Schettler et al. 2011). The hydroxyl content was below the IR detection limits (i.e., $X_{OH} < 0.01$) for all but one sample (APS-26 with $X_{OH} < 0.03$) (Schettler et al. 2011).

TABLE 3. Average compositions of 19 synthetic anhydrous apatite samples determined by EPMA*

Sample	F (%)	Cl (%)	P_2O_5 (%)	CaO (%)	–O=F	–O=Cl	Total (%)	F	Cl	F + Cl	P	Ca	P + Ca
APS-26	BDL†	6.35 (7)	40.80 (37)	53.63 (45)	–	1.43	99.36	–	0.938	0.938	3.008	5.005	8.013
APS-31	BDL	6.22 (6)	40.56 (35)	53.36 (33)	–	1.40	98.73	–	0.895	0.895	3.007	5.007	8.014
APS-24	0.13 (8)	6.27 (6)	40.97 (39)	54.05 (44)	0.06	1.41	99.95	0.036	0.920	0.956	3.003	5.014	8.017
APS-30	0.25 (6)	5.88 (9)	40.86 (26)	53.87 (29)	0.11	1.33	99.43	0.069	0.867	0.936	3.006	5.016	8.023
APS-15	0.35 (5)	5.70 (9)	40.93 (46)	54.19 (33)	0.15	1.29	99.73	0.097	0.836	0.933	3.001	5.030	8.031
APS-29	0.59 (7)	5.16 (13)	41.34 (34)	54.05 (54)	0.25	1.16	99.73	0.162	0.755	0.916	3.019	4.995	8.014
APS-16	0.92 (8)	4.64 (10)	41.11 (30)	54.16 (45)	0.39	1.05	99.39	0.250	0.679	0.929	3.008	5.016	8.023
APS-36	1.12 (13)	4.34 (25)	40.88 (44)	54.00 (44)	0.47	0.98	98.89	0.307	0.638	0.944	3.003	5.020	8.023
APS-28	1.45 (9)	3.64 (13)	41.32 (32)	54.31 (64)	0.61	0.82	99.29	0.395	0.531	0.927	3.011	5.009	8.020
APS-23	1.36 (8)	3.97 (16)	41.37 (28)	54.39 (46)	0.57	0.90	99.62	0.370	0.577	0.947	3.008	5.006	8.014
APS-35	1.48 (8)	3.85 (11)	41.29 (29)	54.02 (40)	0.62	0.87	99.15	0.403	0.563	0.965	3.012	4.988	8.000
APS-23a	1.51 (7)	3.67 (13)	41.30 (39)	54.62 (17)	0.64	0.83	99.64	0.410	0.534	0.944	3.002	5.024	8.026
APS-17	2.09 (12)	2.72 (8)	41.65 (31)	54.82 (52)	0.88	0.61	99.79	0.562	0.393	0.955	3.006	5.007	8.013
APS-34	1.90 (14)	3.02 (18)	41.67 (34)	54.54 (32)	0.80	0.68	99.65	0.515	0.437	0.951	3.013	4.992	8.005
APS-33	2.16 (15)	2.47 (12)	41.68 (23)	54.69 (60)	0.91	0.56	99.53	0.584	0.357	0.941	3.011	5.001	8.013
APS-27	2.27 (12)	2.28 (14)	41.74 (29)	54.73 (58)	0.95	0.51	99.54	0.611	0.329	0.940	3.012	4.999	8.012
APS-20	2.97 (10)	1.33 (6)	41.99 (23)	55.02 (35)	1.25	0.30	99.75	0.794	0.190	0.984	3.008	4.989	7.996
APS-21	3.38 (12)	0.75 (9)	42.15 (22)	54.92 (37)	1.42	0.17	99.61	1.011	0.001	1.012	3.008	4.973	7.982
APS-25	3.80 (12)	BDL	42.30 (34)	55.24 (51)	1.60	–	99.74	0.902	–	0.902	3.011	4.967	7.978

Note: Errors are 1σ standard deviation about the means. Data given in oxide wt% and in apfu; stoichiometry calculated with 13 O atoms.
* Mean EPMA results of 6–10 analyses. EPMA operating conditions: 10 kV accelerating voltage, 4 nA beam current, 10 µm spot, and apatite's *c*-axis perpendicular to the electron beam. Counting times are 60 s for F and Cl and 30 s for Ca and P.
† BDL = below detection limit.

TABLE 4. Average compositions of 19 synthetic anhydrous apatite samples determined by wet-chemical analysis*

Sample	F (%)	Cl (%)	P_2O_5 (%)	CaO (%)	–O=F	–O=Cl	Total (%)	F	Cl	F + Cl	P	Ca	P + Ca
APS-26	0.01	6.44 (6)	40.54 (20)	53.27 (28)	0.00	1.45	98.80	0.003	0.956	0.959	3.007	5.002	8.009
APS-31	0.06	6.34 (9)	40.59 (10)	53.71 (13)	0.03	1.43	99.24	0.017	0.938	0.955	3.000	5.024	8.023
APS-24	0.14 (1)	6.25 (2)	40.64 (20)	53.59 (33)	0.06	1.41	99.15	0.039	0.925	0.963	3.003	5.012	8.014
APS-30	0.21 (1)	6.07 (9)	40.47 (25)	53.50 (38)	0.09	1.37	98.79	0.058	0.901	0.959	3.000	5.020	8.020
APS-15	0.30	5.84 (3)	40.50 (28)	53.62 (50)	0.13	1.32	98.82	0.083	0.866	0.949	3.000	5.027	8.026
APS-29	0.58 (3)	5.17 (5)	40.70 (12)	53.81 (26)	0.24	1.17	98.85	0.160	0.764	0.924	3.004	5.027	8.032
APS-16	0.89 (2)	4.38 (13)	40.77 (32)	53.57 (59)	0.37	0.99	98.25	0.246	0.649	0.894	3.015	5.015	8.030
APS-36	1.37 (4)	4.59 (16)	41.05 (11)	54.19 (8)	0.58	1.04	99.59	0.373	0.670	1.043	2.992	4.999	7.991
APS-28	1.47 (7)	3.53 (12)	40.98 (17)	53.98 (15)	0.62	0.80	98.54	0.403	0.519	0.922	3.009	5.017	8.026
APS-23	1.50 (12)	3.67 (35)	41.71 (60)	55.06 (70)	0.63	0.83	100.48	0.404	0.529	0.933	3.005	5.021	8.026
APS-35†	1.57	3.66	40.56	53.53	0.66	0.83	97.83	0.434	0.542	0.976	3.000	5.012	8.012
APS-23a†	1.54	3.66	40.71	53.83	0.65	0.83	98.27	0.424	0.540	0.964	2.999	5.020	8.019
APS-17	2.05 (8)	2.78 (5)	41.04 (2)	54.05 (13)	0.86	0.63	98.43	0.560	0.407	0.968	3.004	5.007	8.011
APS-34‡	2.07	2.92	40.96	54.04	0.87	0.66	98.46	0.566	0.428	0.994	2.998	5.007	8.005
APS-33	2.22 (4)	2.51 (2)	41.58 (48)	54.55	0.93	0.57	99.36	0.600	0.364	0.964	3.009	4.996	8.005
APS-27	2.46 (6)	2.28 (3)	41.56 (8)	54.48 (12)	1.04	0.51	99.23	0.665	0.330	0.995	3.006	4.988	7.994
APS-20	3.08 (6)	1.21 (5)	41.36 (28)	53.59 (110)	1.30	0.27	97.67	0.839	0.177	1.016	3.017	4.948	7.966
APS-21	3.32 (5)	0.77 (2)	41.90 (24)	55.04 (27)	1.40	0.17	99.46	0.889	0.110	0.999	3.003	4.993	7.996
APS-25	3.77 (5)	0.01 (2)	41.51 (49)	54.74 (58)	1.59	0.00	98.44	1.016	0.001	1.018	2.996	5.001	7.997

Note: Errors are 1σ standard deviation about the means. Data given in oxide wt% and in apfu; stoichiometry calculated with 13 O atoms.
* Wet-chemical data from Schettler et al. (2011). Results are the mean of three analyses.
† Mean of two analyses.
‡ Result of one analysis.

Sample preparation for EPMA

The fluor-chlorapatites are euhedral to semi-euhedral hexagonal crystals that are 1 to 6 mm in length along the *c*-axis and 1 to 3 mm wide. Two grains from each of the samples APS-21, APS-27, APS-35, APS-16, and APS-26 were embedded in epoxy: one with the *c*-axis oriented parallel to the polished surface and one with the *c*-axis oriented perpendicular to the surface. The grain surfaces were ground down with silicon carbide papers and polished with an aqueous slurry of 1 µm alumina powder followed by a slurry of 0.3 µm alumina powder. The grain mounts were placed in an ultrasonic water bath to remove the alumina powder, cleaned with isopropyl alcohol, and coated with a ca. 20 nm thick layer of carbon. The thickness of the C coating was assessed by the color of a brass disk, which was coated along with the samples. The color change on the disk surface varies with the thickness of the C coat, and a purple hue roughly indicates a ca. 20 nm thick coat. In addition, the standards and samples were coated simultaneously to ensure that thickness of the C coat was equal on all standards and samples. This was necessary because the thickness of the C coat can affect the fluorine X-ray counts emitted from the sample (Kerrick et al. 1973). Between each EPMA session, the mounts were re-polished, removing at least 10 µm of surface material, and re-coated with C. This was done because the C coat could have been damaged and because the chemical composition of the apatites, specifically the halogen concentrations, could have been altered in areas that had been exposed to the electron beam (Stormer et al. 1993).

EPMA methods for testing time-dependent intensity variations of F and Cl in apatite

All EPMA were done on a CAMECA SX100 at the American Museum of Natural History. Fluorine, chlorine, calcium, and phosphorous *K*α X-rays emitted from the fluor-chlorapatite samples were analyzed with wavelength-dispersive spectrometry. The EPMA-operating conditions tested are delineated in Table 1. The accelerating potentials investigated are 7, 10, and 15 kV; the beam currents tested are 4, 10, and 15 nA; and the electron-beam diameter was varied between 2, 5, and 10 µm. Each combination of operating conditions was tested on 2 to 4 locations on each sample, with the apatites oriented with their *c*-axes both parallel and perpendicular to the incident electron beam.

The F*K*α X-rays were analyzed with a synthetic "pseudocrystal" diffractor, PC0 (W-Si interlayer with 2d = 45 Å), and Cl*K*α X-rays were analyzed using a high-intensity LPET crystal (large pentaerythritol; 2d = 8.75 Å). The Ca*K*α X-rays were analyzed with a standard PET crystal (pentaerythritol; 2d = 8.75 Å) and P*K*α X-rays were analyzed with a TAP crystal (thallium acid phthalate, 2d = 25.75 Å).

We note that analyzing P on a PET crystal may be preferred because of potential overlapping lower order Ca*K*β lines with P when using TAP (G. Morgan, personal comm.). The standard material used for F analysis was MgF_2, chosen because it contains a high concentration of F (60.98 wt% F, based on stoichiometry), because it was demonstrated previously (Webster et al. 2009) to determine accurate F concentrations in the Durango and Wilberforce apatites and in other F-bearing minerals and glasses by EPMA, and because the peak position of F was found to be the same as in the synthetic apatite samples. The background offsets used for F were ±0.01700 sin θ (~0.75 Å). The standard used for Cl was natural boracite ($Mg_3B_7O_{13}Cl$) because it contains a high concentration of Cl (9.04 wt% Cl based on mineral stoichiometry) and because prior investigation (Webster et al. 2009) proved $Mg_3B_7O_{13}Cl$ returns accurate Cl concentrations for Cl-bearing minerals and glasses by EPMA; the background offsets were ±0.00600 sin θ (+0.05–0.06 Å). The standard used for Ca and P was a synthetic anhydrous apatite that contains 54.48 wt% CaO and 41.62 wt% P_2O_5 based on wet-chemical analyses (Schettler et al. 2011). The background of Ca was determined using a single offset of +0.00700 sin θ (~0.06 Å) and a slope of 1.1 to account for a sloped background. Similarly, P*K*α was counted using a single background offset of +0.00550 (~0.13 Å) and a slope of 1.2.

The X-ray count rate data were collected using the automated "Time Zero Intercept" function in the CAMECA PeakSight software. This application records the number of X-rays counted in a selected time interval, with a maximum number of 30 sub-counting intervals. If more than 30 sub-counting intervals were required, consecutive analyses were performed in the same location on the apatite surface. The total background counting times were set at 1 s each to minimize the time the beam irradiated the sample without counting the emitted X-rays at their peak positions. For tests including a 15 nA beam current, the sub-counting intervals were 5 s, and for tests using 4 and 10 nA, the sub-counting intervals were 10 s. We note that there is a 1 to 2 s delay in counting, between each interval, while the beam continuously irradiates the sample. This counting delay is unpreventable in the CAMECA system and is present in the data collected using the automated Time Zero Intercept function.

The following sections detail the X-ray count rate data with cumulative beam exposure time for various EPMA operating conditions and apatite compositions. The halogen concentrations given for each sample are the wet-chemical analyses, unless otherwise stated.

Results

Time-dependent X-ray intensity variation of F and Cl as a function of crystal orientation

The results of our analytical tests on the influence of apatite grain orientation are consistent qualitatively with those of prior research. Stormer et al. (1993) observed dramatic changes in the time-dependent intensity (TDI) of F and Cl X-rays during EPMA of apatite crystals that are oriented with the *c*-axis parallel to the incident electron beam (Table 1). Specifically, the *K*α X-ray intensity for F in the Durango apatite increases by 100% in the first 60 to 120 s when using 15 kV, 15 nA, and a 5 µm diameter spot. Conversely, if the crystal is oriented with the *c*-axis perpendicular to the electron beam, the count rate increases by only 20% in the first 300 s. Stormer and Pierson (1993) further showed that the apparent F concentration in Durango apatite measured by EPMA when the crystal's *c*-axis was oriented both 44° and 67° from the electron beam significantly exceeded the known F concentration.

The effect of crystal orientation on the variation in X-ray count rates of the halogens in F-rich and Cl-rich apatite is shown in Figure 1. With EPMA conditions of 10 kV, 4 nA, and using a 10 µm spot, the F X-ray count rates of apatite APS-21 with 3.32 wt% F increase 60–70% in the first 300–500 s when the apatite's *c*-axis is parallel to the electron beam (Fig. 1a). Conversely, the F X-ray count rates are constant for 600 s if the crystal is oriented perpendicular to the electron beam with these operating conditions. The Cl X-ray count rates also vary with respect to crystallographic orientation. The Cl X-ray count rates from apatite sample APS-26 with 6.44 wt% Cl decrease by 15% in the first 100–120 s and then decrease sharply by ca. 60% at 300 s when the analysis is conducted with the grain's *c*-axis parallel to the electron beam. When the analysis is performed on the crystal with its *c*-axis perpendicular to the electron beam, the Cl X-ray count rates stay constant for 600 s (Fig. 1b). It is also important to bear in mind that the initial Cl X-ray count rates in the first 10 s subcounting intervals vary with regard to crystal orientation: the count rates are 8% higher in analyses performed with the mineral *c*-axis parallel to the electron beam compared to the analyses conducted on grains oriented perpendicular to the beam. In summary, we note that the F and Cl X-ray count rates are constant over 600 s of analysis in all five samples APS-21, APS-27, APS-35, APS-16, and APS-26 when analyzed with the *c*-axis perpendicular to the beam, but conversely, the variations

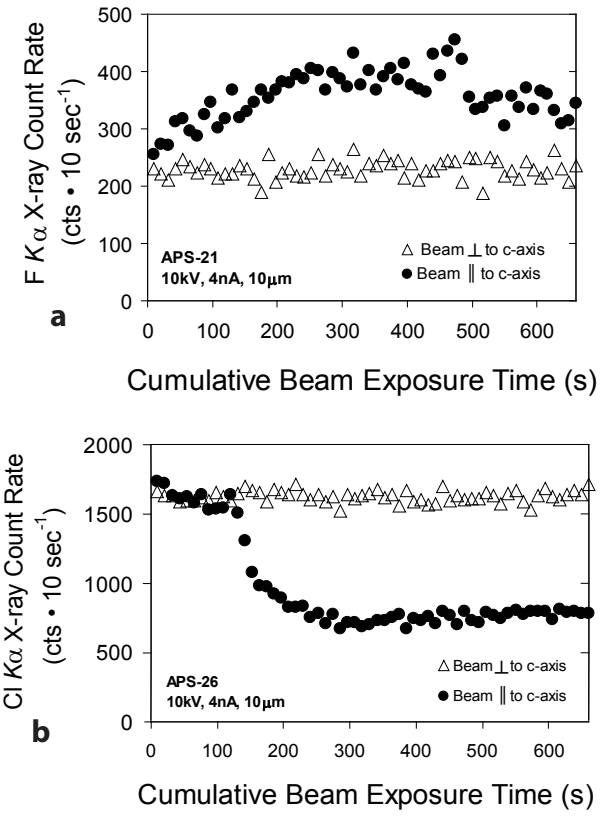

Figure 1. Plots showing the effect of crystal orientation on F (**a**) and Cl (**b**) *K*α X-ray count rates in synthetic, anhydrous F-rich and Cl-rich apatite, respectively, vs. beam exposure time. Samples analyzed by EPMA with 10 kV accelerating voltage, 4 nA beam current, 10 µm diameter spot, and with crystals oriented both with the *c*-axis perpendicular and parallel to the electron beam. Each point represents the total number of X-ray counts in a given 10 s interval, and each interval is followed by a 1–2 s delay in counting (estimated at 1 s) while the beam continuously irradiates the sample. The F and Cl *K*α X-ray count rates vary dramatically when the samples are analyzed parallel to the *c*-axis, with these analytical conditions, whereas the count rates are constant when the apatites are analyzed with the *c*-axis perpendicular to the electron beam.

in F and Cl X-ray count rates are different for each apatite composition when analyses are conducted with the *c*-axis oriented parallel to the beam.

Time-dependent X-ray intensity variation of halogens as a function of apatite composition

The TDI variations for F and Cl in fluor-chlorapatite with EPMA operating conditions of 10 kV accelerating potential, 15 nA current, 10 µm diameter spot, and with the crystal *c*-axis parallel to the incident electron beam are strongly affected by apatite composition (Fig. 2). Because changes in halogen X-ray intensities are minimal when analyses are performed with these EPMA-operating conditions on apatite grains oriented with their *c*-axis perpendicular to the electron beam, the influence of apatite composition will only be evident in analyses conducted on samples oriented with the *c*-axis parallel to the electron beam, and therefore these are the only results presented below. Note that each sample was analyzed in 3 or 4 locations.

The X-ray intensity for F increases in the first 100–350 s of analysis and decreases thereafter for each of the apatites studied (Fig. 2a). With APS-21 (3.32 wt% F), the most F-rich apatite examined, the F X-ray intensity increases by 30–50%, which is then followed by a drop to levels below the initial intensity. Similarly, in APS-27 containing 2.46 wt% F, the F count rates increase by 30–50% and subsequently decrease to a rate below the initial rate. In APS-35 (1.57 wt% F), the F X-ray intensity increases by 60–100%, which is the largest increase in intensity, and the F X-ray counts in APS-16 (0.9 wt% F) increase by 10–60% in the first 100 s.

The X-ray TDI variations for Cl in these fluor-chlorapatites differ from the behavior observed for fluorine (Fig. 2b). The Cl X-ray intensity in APS-26, with 6.44 wt% Cl, decreases slightly, by just a few percent below initial intensity during the first 100–200 s, then drops significantly after ca. 200 s, and thereafter remains constant at 50–65% less than the initial count rate. In APS-16 (4.38 wt% Cl), the Cl X-ray intensity increases

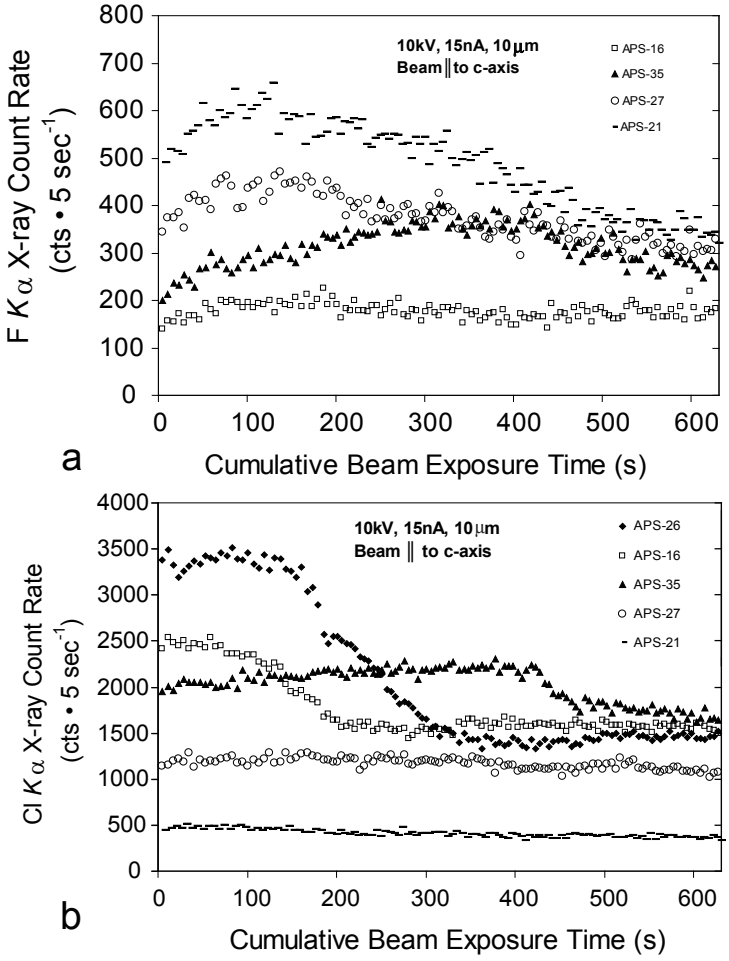

FIGURE 2. Plots showing the F (**a**) and Cl (**b**) *K*α X-ray count rates in synthetic, anhydrous fluor-chlorapatite with varying F and Cl concentrations vs. beam exposure time. Samples analyzed by EPMA with 10 kV accelerating voltage, 15 nA beam current, 10 µm diameter spot, and sample oriented with the *c*-axis parallel to the electron beam. Each point represents the total number of X-ray counts in a given 5 s interval, and each interval is followed by a 1–2 s delay in counting (estimated at 1 s) while the beam continuously irradiates the sample. The F*K*α X-ray count rates increase then decline with beam exposure time, whereas the Cl*K*α X-ray count rates fluctuate irregularly before declining.

minimally in the first 100–200 s of analysis and subsequently decreases sharply to levels about 30% below the initial count rate. In APS-35 (3.66 wt% Cl), the Cl X-ray intensity increases by 20–25% at 400 s then decreases to 5–20% less than the initial intensity. In APS-27 (2.28 wt% Cl), the Cl X-ray intensity remains constant for 300 s then decreases by 20–35% in the following 300 s of analysis. Last, with the lowest-Cl apatite APS-21 (0.77 wt% Cl), the Cl X-ray intensity simply decreases by 20–30% over 600 s of analytical time.

To summarize, for apatite analyses parallel to the crystallographic *c*-axis, the Cl X-ray count rates vary the most in apatite that is the most Cl enriched, and the relationship between F X-ray count rate variation and F concentration in apatite is more complicated. The relative increase in F X-ray counts is lower for APS-21 with 3.32 wt% F than it is with APS-35, which contains 1.57 wt% F.

Effect of accelerating potential on halogen X-ray intensity variation

The accelerating potential used for EPMA of apatite must be selected with care. A review of the literature shows that natural apatite samples are often analyzed with a 15 kV accelerating voltage to produce sufficient overvoltages in REEs and other trace components in apatite. The overall goal, herein, is to select operating conditions that do not alter apatite composition while generating statistically significant counts during analysis of trace components.

Stormer et al. (1993) examined the effect of this operating parameter on F in the Durango apatite and determined that it does not affect the initial X-ray count rate variation that shows increases in intensity during brief periods of beam exposure, but they observed subsequent changes in F X-ray intensity with continued electron beam exposure. Accelerating voltage has a similar effect on the F X-ray intensity in zwieselite-triplite phosphates [i.e., $(Fe^{2+},Mn)_2PO_4(F)$] whereby intensity increases at a similar rate with the use of 5 and 10 kV accelerating voltages in the first 60 s of beam exposure (Fialin and Chopin 2006). After this initial rise, the intensity continues to increase with the use of a 5 kV accelerating voltage but decreases when analyzed with a 10 kV accelerating voltage (Fialin and Chopin 2006).

The accelerating potential applied in our tests had a large effect on the number of Cl$K\alpha$, Ca$K\alpha$, and P$K\alpha$ X-rays emitted per nanoamp of current, and a smaller influence on the number of F$K\alpha$ X-rays emitted from these anhydrous fluor-chlorapatites (Table 2, Fig. 3). The use of a 15 kV accelerating voltage results in a larger number of accumulated Cl, Ca, and P X-ray counts than the use of 7 and 10 kV accelerating potentials (Table 2). The response of F is more complicated. A 10 kV accelerating potential yields a greater number of emitted F X-rays if the apatite grain is oriented with the *c*-axis perpendicular to the incident electron beam, whereas the use of 7, 10, and 15 kV accelerating voltages result in similar numbers of X-rays for F with the beam parallel to the apatite *c*-axis.

The effect of accelerating voltage on Cl intensity is shown in Figure 3 for high-Cl apatite APS-26 with its *c*-axes parallel to the incident electron beam. The Cl X-ray intensity varies differently during the first 20–30 s of beam irradiation, then intensities either gradually decline or remain constant over the following 630 s of beam irradiation. With 15 kV acceleration potential the Cl X-ray intensity declines by 20–30%, and with 10 kV the intensity decreases by 30–40% after 660 s. Although, on average, the Cl X-ray intensity using 7 kV acceleration shows an initial increase, we note considerable variability from one analytical spot to another. In one location the X-ray intensity remained constant over 660 s of analytical time, whereas intensity increased by 16% in a second location vs. decreasing by 56% in a third location. The variability observed at 7 kV acceleration may, at least in part, be due to poor counting statistics resulting from weak peak intensity.

Effect of beam diameter on halogen X-ray intensity variation

Experimentally prepared and natural apatite grains are often quite small in size, and some natural crystals may be strongly zoned (Boyce and Hervig 2008) so it may be necessary to employ a small analytical spot size during in situ analysis of apatite. This analytical issue can be problematic because halogen X-ray count rates vary with EPMA spot size depending on the crystal orientation during analysis. Stormer et al. (1993), for example, showed that decreasing the beam diameter increases the rate at which the F X-ray intensity rises in Durango apatite oriented with the *c*-axis parallel to the electron beam. They also noted that larger spot sizes result in greater increases in F X-ray intensity, but that these increases occur after extensive beam exposure time (Stormer et al. 1993).

We tested the influence of spot size on the TDI variation of halogens in our anhydrous fluor-chlorapatites, and representative results for F behavior are shown in Figure 4. Analyses of apatite grains oriented with their *c*-axes parallel to the incident electron beam and irradiated with a 10 kV accelerating voltage and 4 nA beam current show changes in F X-ray intensity with

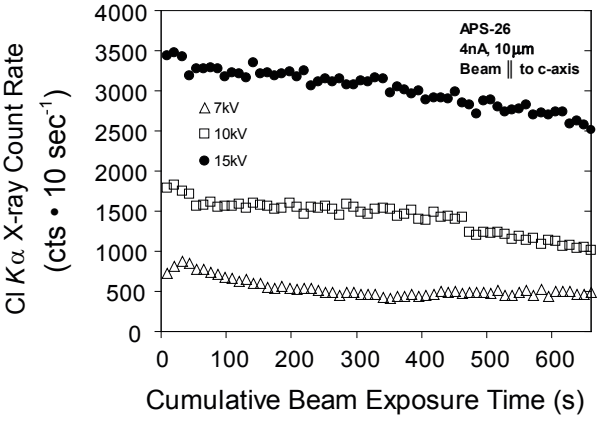

Figure 3. Plot showing the effect of 7, 10, and 15 kV acclerating potentials on Cl$K\alpha$ X-ray count rates in chlorapatite sample APS-26 containing 6.44 wt% Cl and measured against beam exposure time with the beam directed parallel to the crystallographic *c*-axis. A 15 kV accelerating potential results in more emitted Cl$K\alpha$ X-rays and less count rate variation in chlorapatite than 7 and 10 kV accelerating potentials. Each point represents the total number of X-ray counts in a given 10 s interval, and each interval is followed by a 1–2 s delay in counting (estimated at 1 s) while the beam continuously irradiates the sample.

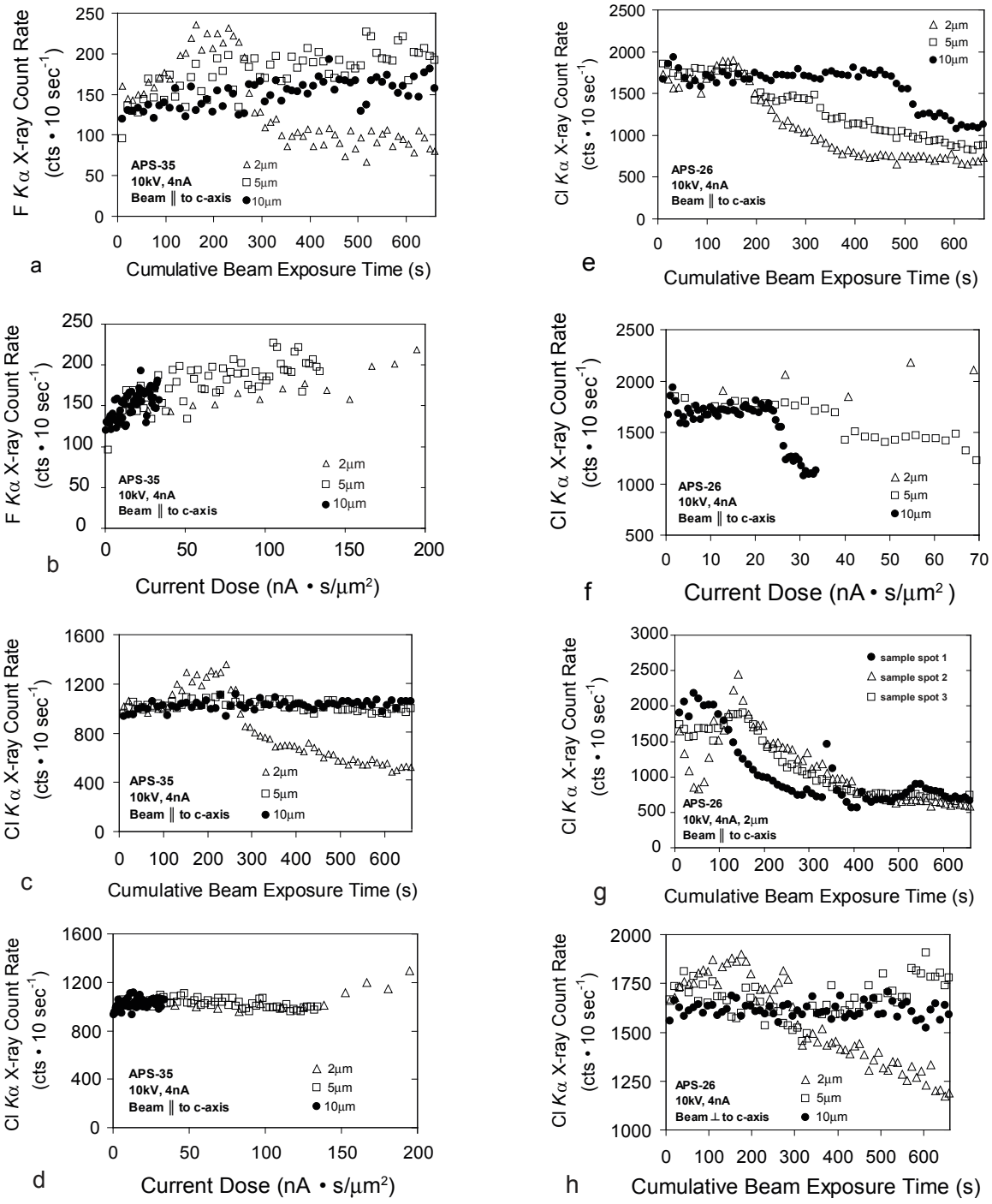

FIGURE 4. Plot showing the effect of 2, 5, and 10 μm diameter spots on F (**a**) and Cl (**c**) *K*α X-ray count rates in APS-35 (1.57 wt% F and 3.66 wt% Cl) when the beam is parallel to the *c*-axis, and plotted against beam exposure time. Plots F (**b**) and Cl (**d**) show *K*α X-ray count rates in APS-35 with varying spot sizes and plotted against the current dose, which describes the beam current density multiplied by the beam exposure time (s). Also shown are: the effect of spot size on Cl*K*α X-ray count rates in chlorapatite sample APS-26 (6.33 wt% Cl) when the beam is parallel to the *c*-axis, and plotted against beam exposure time (**e**) and current dose (**f**); the variability of Cl*K*α X-ray count rates on a crystal oriented with the c-axis parallel to the beam and analyzed with a 2 μm beam diameter spot in different locations on the same polished surface (**g**); and the effect of spot size on Cl*K*α X-ray count rates when the beam is perpendicular to the *c*-axis and plotted against analytical time (**h**). Larger spot sizes (e.g., 5 and 10 μm beam diameters), and therefore smaller current densities, result in more constant F and Cl X-ray count rates with cumulative beam exposure time than smaller spot sizes (e.g., 2 μm diameter). Each point represents the total number of X-ray counts in a given 10 s interval, and each interval is followed by a 1–2 s delay in counting (estimated at 1 s) while the beam continuously irradiates the sample.

2, 5, and 10 μm diameter spots. The F X-ray count rate varies more quickly with the use of a 2 μm diameter spot, than with a 5 or 10 μm diameter spot (Fig. 4a). When analyzed with a 2 μm spot electron beam, the F X-ray count rate in APS-35 (1.57 wt% F) remains constant for 100 s before increasing 20–70% between 100 and 300 s and then declines precipitously to levels below the initial value. Conversely, the F X-ray intensity increases steadily using 5 and 10 μm diameter spots, with the magnitude of change being smaller with the use of a 10 μm spot. Figure 4b shows the same F X-ray data but plots it against beam current dosage, and we employ this metric because it conveys the cumulative number of electrons that have impinged upon on an area of sample in a given time interval. Beam dosage describes the current density (beam current divided by the area analyzed) multiplied by the beam irradiation time and it is expressed as $nA \cdot s/\mu m^2$. When the F X-ray data for 2, 5, and 10 μm spots are normalized to current dosage, the slopes of all three trends generally align, indicating that this is a salient variable that affects the F X-ray count rate changes with progressive analytical (beam exposure) time (Fig. 4b).

The Cl X-ray count rates from APS-35 behave in a similar fashion to those of F in APS-35 (Figs. 4c and 4d). The Cl X-ray count rates from APS-26 (6.44 wt% Cl) fluctuate in the first 200 s before declining in the following 400 s for all spot sizes tested, and the count rate declines most rapidly with the use of a 2 μm diameter spot, followed by a 5 μm spot, and last by a 10 μm spot (Fig. 4e). When these Cl X-ray data are plotted against the current dosage, the trends diverge suggesting that current flux per unit area is not the only controlling factor in the time-dependent variation in Cl-rich apatite (Fig. 4f). Variation among individual analyses could be a factor, for example. In fact, Figure 4g shows that Cl X-ray intensity data vary when analyzed on different locations on the surface of single homogenous apatite grain with use of a 2 μm spot.

As a representative example of the effect of spot size on halogens in fluor-chlorapatite oriented with the *c*-axis perpendicular to the electron beam, Figure 4h shows the effect of beam diameter on analytical tests of Cl-rich apatite APS-26. Samples analyzed perpendicular to the *c*-axis with 4 nA, 10 kV, and a 5 or a 10 μm beam diameter spot result in a constant count rate of X-rays over 660 s of cumulative beam exposure time, which is equivalent to 33.6 $nA \cdot s/\mu m^2$ for the 10 μm diameter spot and 134 $nA \cdot s/\mu m^2$ for the 5 μm diameter spot.

In summary, greater beam densities result in increasingly variable X-ray count rates. Reducing the current density by enlarging the beam diameter results in more constant X-ray count rates, and this is true for analyses involving both of the primary crystallographic orientations studied (i.e., parallel and perpendicular to the *c*-axis).

Effect of beam current on halogen X-ray intensity variation

With regard to selecting an optimal analytical strategy for apatite analysis, increasing the beam current will increase the count rates and, therefore, improve the precision of analysis only to the extent that it does not negatively affect the X-ray intensity variation associated with progressive beam exposure (e.g., Stormer and Pierson 1993). Therefore, we also have tested the outcome of varying the beam current (4, 10, or 15 nA) on the resulting halogen X-ray intensities for F- and Cl-enriched apatites analyzed with the electron beam parallel to their *c*-axes.

Using a 10 kV accelerating voltage and 10 μm spot on F-rich apatite APS-21, the F X-ray intensity rises rapidly and then falls when analyzed with a 15 nA current (Fig. 5a). The intensity increases more slowly with the use of 10 and 4 nA beam currents at these conditions (Fig. 5a). The beam current dose determines the shape of the F X-ray count rate curves in F-rich apatite (Fig. 5b). Higher currents accelerate the changes in F X-ray intensity, but do not dramatically change the shape of the curve.

The intensities of Cl X-rays also fluctuate as the beam current varies from 4 to 15 nA, and the count rates are most constant and therefore most stable at 4 nA. Intensities in Cl-rich apatite APS-26 rapidly decrease and subsequently increase during initial beam exposure (100 s), before generally declining with subsequent and extended beam exposure (Fig. 5c). When X-ray intensities are plotted against beam current dosage (Fig. 5d), the curves for Cl using different currents are similar at low dosages, especially for the 4 and 10 nA currents.

Summary of TDI tests

Optimal analytical results for F and Cl were achieved when apatite grains are analyzed perpendicular to their *c*-axes and when using relatively low beam currents, relatively low accelerating potentials, and larger defocused beam spot sizes. These results are consistent qualitatively with prior observations of Stormer et al. (1993) and Stormer and Pierson (1993). However, our tests also indicate that the quality of electron microprobe analyses of apatite grains oriented with their *c*-axes parallel to the electron beam is best for apatite samples having intermediate halogen contents (i.e., the results become increasingly inaccurate as the pure-F and pure-Cl end-member compositions are approached).

An optimized electron probe microanalysis technique

Based upon the preceding results, we derive an optimized procedure for analyzing the principal constituents of fluor-chlorapatites. The accelerating voltage selected is 10 kV, to maximize the F*K*α X-ray intensity (Table 2) while also producing sufficient overvoltage for Cl, P, and Ca X-rays. A beam current of 4 nA, measured at the Faraday cup, was selected because this low current value causes less TDI variation in F and Cl while simultaneously generating adequate F, Cl, P, and Ca X-ray intensities. A 10 μm diameter spot size minimizes the intensity variation by reducing the current density. All of the principal elements, Ca, P, F, and Cl, are analyzed simultaneously using the methods and standards described above. Counting times for Ca and P X-rays of 30 s on peak and 15 on background provide adequate statistics for these components. Counting times for F and Cl X-rays are 60 s on peak for analyses perpendicular to the *c*-axis of apatite and 30 s on peak for analyses parallel to the *c*-axis. Longer counting times are used on samples oriented with the *c*-axis perpendicular to the beam, as opposed to parallel to it, because there is less TDI variability in this orientation. These differing count times yield the maximum numbers of accumulated counts prior to significant intensity variation for each crystal orientation. Test analyses conducted perpendicular to the *c*-axis with 60 s counting times yielded minimum detection

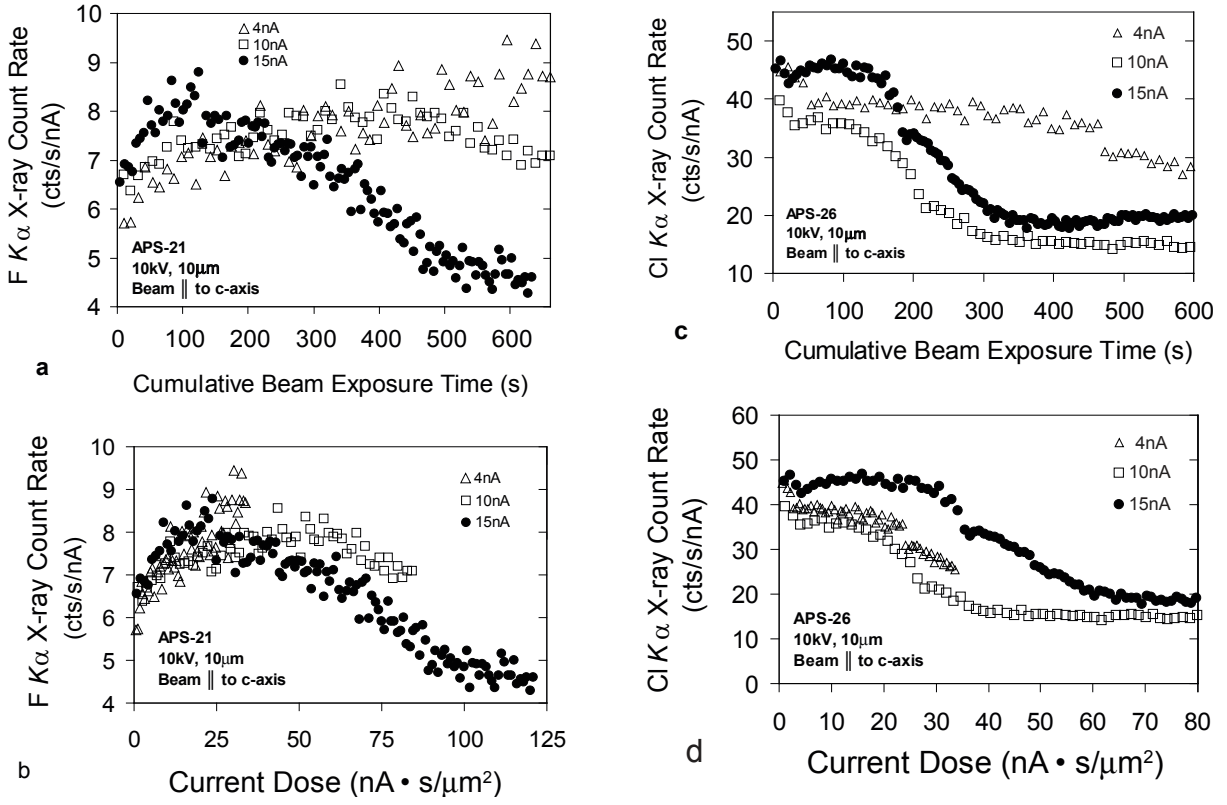

FIGURE 5. Plots showing F*K*α X-ray counts per second per nA in F-rich apatite APS-21 (3.32 wt% F) plotted against beam exposure time (**a**) and current dose (**b**) for 4, 10, and 15 nA beam currents. Plots showing the Cl*K*α X-ray counts per second per nA in chlorapatite APS-26 containing 6.44 wt% Cl plotted against beam exposure time (**c**) and current dose (**d**) for various electron beam currents. All samples were analyzed with the beam parallel to the *c*-axis. Higher currents accelerate the changes in F and Cl X-ray count rates; F X-ray count rates rise and Cl X-ray count rates decline more slowly with the use of 4 and 10 nA currents than with a 15 nA current. Current dose describes the beam current density multiplied by the beam exposure time. The points represent counts/s/nA in a given 10 s interval for the 4 and 10 nA current data and a 5 s interval for the 15 nA current data, and each interval (i.e., data point) is followed by a 1–2 s delay in counting (estimated at 1 s) while the beam continuously irradiates the sample.

limits of 0.12 wt% F and 0.02 wt% Cl with our instrument for analysis performed using the PAP matrix correction procedure (Pouchou and Pichoir 1984).

This methodology was tested by analysis of 19 anhydrous fluor-chlorapatites that span the fluor-chlorapatite solid-solution series, including the 5 samples that were examined previously in the TDI tests of Cl and F (Table 3). The samples were analyzed with the *c*-axes perpendicular to the electron beam in 6–10 spots randomly distributed over the crystal surfaces; these analyses included both rims and cores of the grains (Fig. 6). Also, to evaluate the observed influence of bulk halogen content on EPMA parallel to the crystal *c*-axis, we analyzed 7 of these samples in 3–5 individual spots (Fig. 7). In processing the results, individual analytical data were eliminated if the totals were less than 98.5 or greater than 101.5 wt% after the equivalent of oxygen for halogens was accounted for (i.e., subtracted from the total). Totals that vary much from 100 wt% could be a result of poor focus of the stage on the polished grain surface and/or due to mineral surface imperfections. This constraint is justified because all of the major components present in these relatively anhydrous apatites were analyzed.

Results of optimized EPMA perpendicular to fluor-chlorapatite *c*-axes

Accurate analyses of F and Cl in the 19 synthetic anhydrous fluor-chlorapatites were obtained for grains oriented with their *c*-axis perpendicular to the electron beam while using these analytical methods. The EPMA results for F and Cl correlate extremely well with the wet-chemical analyses and have R^2 values of 0.992 and 0.994, respectively, for all 19 samples (Tables 3 and 4; Figs. 6a and 6b). Accuracy for the halogen-rich apatites, which show a great deal of TDI variations, is shown by comparing the EPMA and wet-chemistry data for the most F-rich and Cl-rich synthetic apatites to the theoretical F and Cl maxima for end-member apatites. Pure end-member fluorapatite theoretically contains 3.76 wt% F based on stoichiometry, and in comparison, sample APS-25 yields 3.80 ± 0.12 wt% F by EPMA and 3.77 ± 0.05 wt% by wet-chemical analysis (Table 4). Likewise, pure chlorapatite theoretically contains 6.81 wt% Cl, whereas the synthetic chlorapatite sample APS-26 yields 6.35 ± 0.07 wt% Cl by EPMA and 6.44 ± 0.06 wt% by wet chemistry. Slight Cl deficiency in the synthetic apatite is attributed to charge balance by oxygen accompanying an oxy-apatite component, as

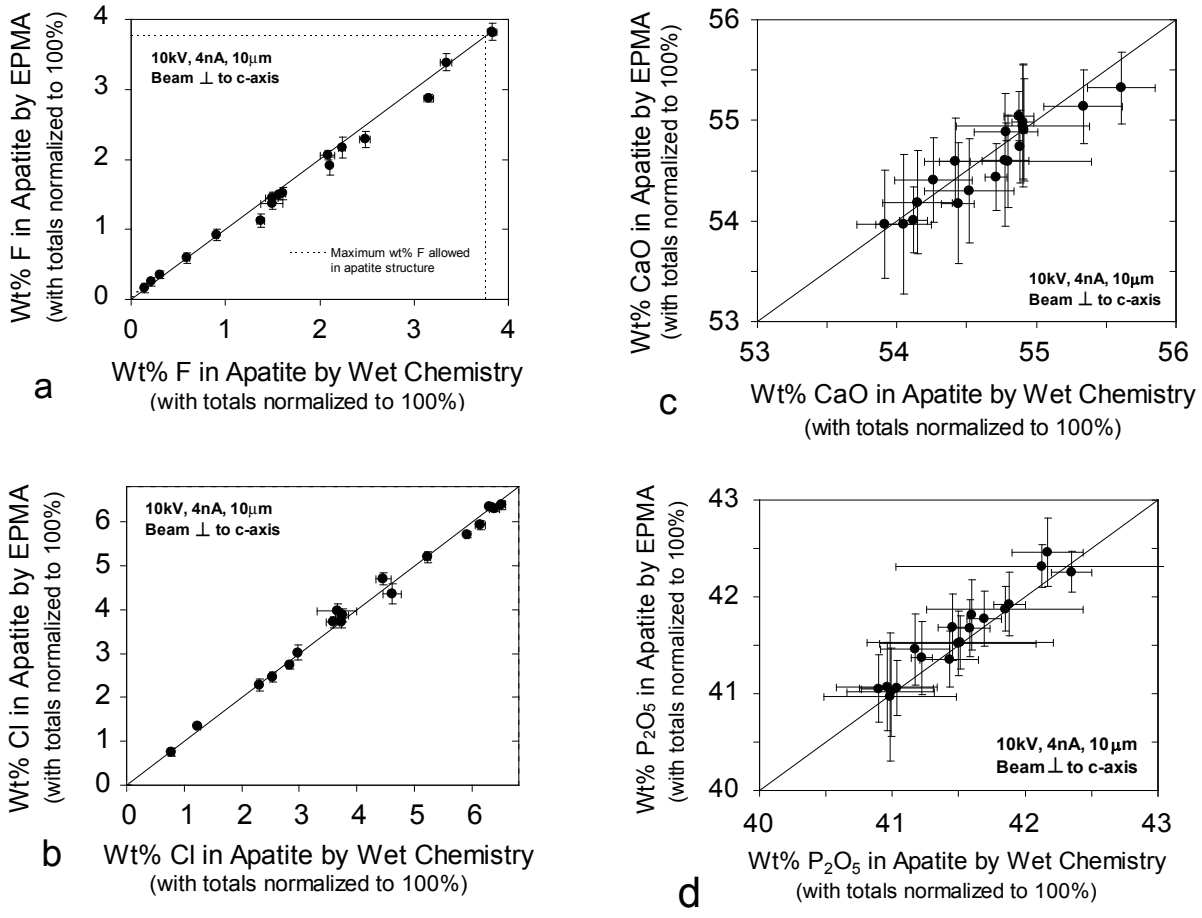

FIGURE 6. Plots showing the concentrations (wt%) of F (**a**), Cl (**b**), CaO (**c**), and P_2O_5 (**d**) in 19 synthetic, anhydrous fluor-chlorapatite samples measured using the optimized EPMA technique of this investigation (10 μm spot, 4 nA beam current, 10 kV accelerating voltage, beam perpendicular to the *c*-axis of the apatite grains, 60 s counting time for F and Cl and 30 s for P and Cl at the peak positions) vs. corresponding wet-chemical analyses from Schettler et al. (2011). The solid line represents a one-to-one relationship and is not a fit to the data. The dashed line (**a**) represents the maximum allowed F in apatite based on mineral stoichiometry. The EPMA results agree very closely with the wet-chemical analyses. Each sample analyzed in 6–10 locations and the error bars represent 1σ standard deviation about the mean. The data have been normalized such that the analytical totals are 100 wt%. Unnormalized data are shown in Tables 3 and 4.

noted previously for the Cl-rich apatites (Schettler et al. 2011).

The EPMA data for CaO (Fig. 6c) and P_2O_5 (Fig. 6d) agree with the wet-chemical analyses (Tables 3 and 4). Importantly, the calculated structural formulas, based on these analyses, are closely consistent with stoichiometric constraints (Table 3).

Durango apatite with the crystal oriented with the *c*-axis perpendicular to the electron beam was analyzed as a secondary standard along with the synthetic fluor-chlorapatites using the same analytical methods. The average of 9 analyses return: 3.40 ± 0.13 wt% F, 0.42 ± 0.01 wt% Cl, 53.83 ± 0.26 wt% CaO, and 41.08 ± 0.30 wt% P_2O_5 with a total of 98.73 wt%, which agree well with the reported wet-chemical composition of 3.53 wt% F, 0.41 wt% Cl, 54.02 wt% CaO, and 40.78 wt% P_2O_5 (with equivalent analytical totals of 98.74 wt%, cf. Jarosewich et al. 1980).

The relative accuracy (RA) obtained for F, determined from a Poissan distribution as $1/\sqrt{N}$ where N is the total number of accumulated counts above background, varied from 13 to 3% in F-poor and F-rich apatite over the full range of compositions analyzed. The relative accuracies for Cl are better than for F because of the higher intensity of Cl by EPMA. The relative accuracies for Cl range from 3% to <l% in Cl-poor and Cl-rich apatite, respectively. As an example of a complete analysis, the mean total peak X-ray counts above background for APS-35 are: 561 for F yielding an RA of 4.2% at 1.5 wt% F; 5885 for Cl yielding an RA of 1.3% (3.83 wt% Cl); 14 135 for Ca yielding an RA of 0.8% (53.79 wt% CaO); and 22 686 for P, providing an RA of 0.7% (41.19 wt% P_2O_5).

Results of optimized EPMA parallel to fluor-chlorapatite *c*-axes

The comparison of wet-chemical analyses vs. EPMA conducted perpendicular to the apatite *c*-axis shows minor to negligible differences in the F and Cl contents that are a random function of bulk halogen concentrations (Fig. 6). Conversely, halogen contents obtained by EPMA performed with analyses parallel to the crystallographic *c*-axis diverge from the wet-chemical

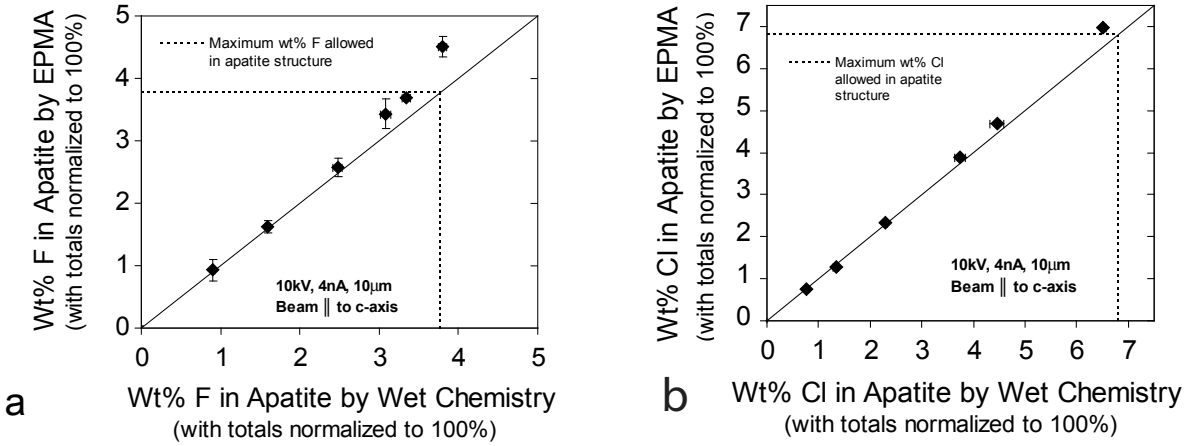

FIGURE 7. Plots showing the F (**a**) and Cl (**b**) concentrations (wt%) in synthetic, anhydrous fluor-chlorapatites measured by EPMA vs. corresponding wet-chemical analyses from Schettler et al. (2011). Samples analyzed with a 10 kV accelerating potential, 4 nA beam current, 10 μm beam diameter on the sample, and with the apatite crystallographic *c*-axis parallel to the incident electron beam. Counting times are 30 s on the peak positions. The solid line represents a one-to-one relationship and not a fit to the data. The dashed lines in **a** and **b** represent the maximum allowed F and Cl contents in apatite, respectively, based on mineral stoichiometry. Fluorine and Cl EMPA concentrations in fluor-chlorapatite with intermediate compositions agree well with the wet-chemical analyses, whereas end-members and near-end-member compositions show statistically significant discrepancies between EPMA data and wet-chemical analyses. Each point is the mean of a sample analyzed in 3–5 locations and the error bars represent 1σ standard deviation about the mean (symbol may be larger than the error). The data have been normalized such that the analytical totals are 100 wt%.

values at high F or Cl contents (Fig. 7). For example, EPMA of fluorapatite sample APS-25 in this orientation yields 4.42 ± 0.25 wt% F vs. its nominal 3.80 ± 0.12 wt% F (Fig. 7a; Tables 3 and 4). Chlorine-rich sample APS-26 results in 6.93 ± 0.10 wt% Cl when the EPMA analysis is conducted with the crystal *c*-axis oriented parallel to the electron beam vs. 6.35 ± 0.07 wt% Cl when the *c*-axis is oriented perpendicular to the beam and 6.44 ± 0.06 wt% Cl by wet-chemical analysis (Fig. 7b, Tables 3 and 4).

It is also noteworthy that analysis of the fluor-chlorapatites with intermediate halogen proportions analyzed with their *c*-axes parallel to the electron beam provides F and Cl concentrations that show good agreement with the wet-chemical analyses and with the analyses performed on crystals oriented with their *c*-axes perpendicular to the beam. For example, analysis of sample APS-35 in this orientation yields 1.62 ± 0.10 wt% F and 3.87 ± 0.13 wt% Cl vs. 1.48 ± 0.08 wt% F and 3.85 ± 0.11 wt% Cl when the analysis is conducted perpendicular the *c*-axis (Fig. 7; Tables 3 and 4). Likewise, the F and Cl concentrations in APS-27 measured by EPMA in both crystallographic orientations and the wet-chemical analyses agree well. The counting times for these analyses were 30 s at the peak positions, which produced a beam dosage of 1.54 nA·s/μm^2. This current dosage caused large changes in the F and Cl TDI and the resulting concentrations in end-member and near-end-member fluor-chlorapatites, but did not produce significant changes in the F and Cl TDI in the intermediate fluor-chlorapatites with their *c*-axes oriented parallel to the electron beam during analysis. Indeed, Figure 1 shows that there is a discrepancy between the Cl X-ray count rates in the first 10 s counting interval for the two crystal orientations, demonstrating a rapid change in the X-ray intensity in end-member apatite. Recall, however, that large variations in the TDI of F and Cl in both end-member and intermediate compositions do occur during relatively long periods of beam exposure and with higher beam currents (Fig. 2) than those that were employed for this optimal method. In fact, the intermediate composition, APS-35, shows the largest relative increase in F X-ray intensity. Yet, accurate analyses of F and Cl are possible in APS-35 that is oriented with its *c*-axis parallel to the electron beam with shorter but analytically appropriate counting times (Fig. 7).

To summarize, these results demonstrate that, contrary to popular wisdom, accurate analyses of some OH-poor apatites can be conducted parallel to the *c*-axis of this mineral with confidence using this protocol and that the initial rate of X-ray intensity variation is higher with end-member apatites than it is in apatites with intermediate halogen-contents. With regard to practical applications of this optimized method, the orientation of apatite grains in thin sections is not always apparent (meaning that one might not trust data collected from apatite grains with unknown crystallographic orientations); however, this issue may not be particularly problematic as long as the apatite is not at or near the end-member, F- or Cl-rich compositions.

FINAL CONSIDERATIONS

Automated time-zero EPMA correction for halogens in apatite

Time-dependent intensity-based correction schemes can extrapolate observed X-ray count rates back to that occurring at the instant an electron beam first contacts the polished surface of any sample, and this approach has been suggested (Stormer et al. 1993) as a method to correct for the variations in X-ray count rates of apatites over analytical time. McCubbin et al. (2010) demonstrate the importance of time-zero corrections when apatites are prohibitively small in size. However, the non-linear nature of the TDI trends presents difficulties in back calculating to the X-ray intensity at zero time. To address this issue, Mc-

Cubbin et al. (2010) monitored the F X-ray count rates with a chart recorder in the EPMA software on a JEOL 8200 electron microprobe and only accepted analyses in which the count rates for which the applied curves were linear and positively sloped, and then extrapolated back to the initial count rate, which was then used to calculate the F concentration.

The "Time Zero Intercept" function used with CAMECA software allows the user to select the number of sub-counting intervals in which the peak position counting time is divided. The X-rays are counted in each interval, and then the count rate is extrapolated back to time zero when the electron beam is first exposed to the sample. In our tests conducted using the automated "Time Zero Intercept," this sub-counting application did not yield more accurate results than analyses performed without using the function. Short sub-counting intervals do not improve the accuracy of the test. Furthermore, Morgan and London (2005) point out that there is often a delay in X-ray counting after the electron beam has come into initial contact with the sample, and incipient changes in X-ray intensity that may not be detected. Therefore, we do not recommend using an automated correction procedure with this instrument and its operating software.

Modeling the TDI curves for F and Cl is also problematic because the shape of the resulting curves is a function of the fluor-chlorapatite composition (Fig. 2). However, use of a chart recorder to monitor TDI would be appropriate to discriminate analyses that show no TDI change and analyses showing X-ray count rate variations can be eliminated.

Recommendations for EPMA of apatite

Because there are time-dependent variations in the X-ray counts (and, hence, in the measured element concentrations with EPMA), it is advisable not to expose the apatite to an electron beam prior to analysis (i.e., to identify and locate apatite crystals in thin sections using BSE imaging). It is also important to limit counting times and to analyze the least-stable primary components in apatite, including F, Cl, Ca, and P, first during the analytical scheme, and subsequently to analyze other minor and trace elements that exhibit more stable behavior while exposed to an electron beam. Pyle et al. (2002) also recommended using relatively short analysis times for F, Cl, Ca, and P followed by longer analysis times for trace elements. The use of a 15 kV accelerating voltage, rather than 10 kV as used here, may be useful for most analysts because it produces robust X-ray counts for most elements analyzed, including heavier metals. Moreover, as noted above, this higher accelerating voltage may reduce changes in TDI (Stormer and Pierson 1993).

The research of Stormer et al. (1993) and our work (both of which were conducted with CAMECA microprobes with take-off, X-ray beam angles of 40°) show that the crystallographic orientation of F- and Cl-bearing apatites has a significant effect on the time-dependent X-ray intensities of the halogens. Stormer and Pierson (1993) show that even EPMA of F-rich apatite grains with their *c*-axis oriented 44° from the polished surface result in large TDI variations. Therefore, it is important to interpret EPMA analytical data with regard to the orientation of each apatite grain. Yet, our results also show that with minimal beam current doses, accurate analyses of intermediate fluor-chlorapatites are possible, even when the crystals are oriented with the *c*-axes parallel to the electron beam. An important observation from this investigation is that end-member and near-end-member, anhydrous fluor-chlorapatites exhibit rapid changes in count rates, while intermediate compositions (e.g., APS-16 and APS-35) change more slowly. This new observation allows for accurate analysis of F, Cl, P_2O_5, and CaO—if they are each analyzed first during the analytical scheme and each with a separate spectrometer—while also using short counting times and minimal current doses.

The primary EPMA technique we used to accurately analyze the 19 synthetic apatites composed of only F, Cl, CaO, and P_2O_5 was also effective in accurately analyzing those components in our secondary standard material, the Durango F-rich apatite, which contains 2 wt% REE_2O_3 and minor to trace concentrations of other elements including Si, S, N, and Fe (Jarosewich et al. 1980). This suggests that this EPMA technique should be applicable to natural fluor-chlorapatites with a minor hydroxyl component, given the consistency of the EPMA results of the OH-bearing Durango apatites vs. the wet-chemical data using our optimal analytical protocol. It is important to note that the presence of an Fe peak may interfere with the background of the F peak in the PCO crystal; therefore if Fe is present in relatively high concentrations, the background positions for F should be offset more broadly. Chlorine- and F-rich apatites with minimal hydroxyl components are found in terrestrial rocks and martian meteorites (Treiman et al. 1993; Sautter et al. 2006; McCubbin and Nekvasil 2008; Filiberto and Treiman 2009). Conversely, the application of this technique on apatites that contain substantial OH concentrations should be done with caution since hydrous apatite may not behave in the same fashion as anhydrous apatite under the electron beam.

Acknowledgments

We acknowledge helpful discussions on analytical methodology with Philip Piccoli and Charles Mandeville and thoughtful and detailed reviews by G. Morgan, J.C. Stormer, F. McCubbin, and P. Carpenter on the manuscript. This research was supported by National Science Foundation award EAR-0836741 to J.D.W.

References cited

Boyce, J.W. and Hervig, R.L. (2008) Magmatic degassing histories from apatite volatile stratigraphy. Geology, 36, 63–66.

Boyce, J.W., Liu, Y., Rossman, G.R., Guan, Y., Eiler, J.M., Stolper, E.M., and Taylor, L.A. (2010) Lunar apatite with terrestrial volatile abundances. Nature, 466, 466–469.

Campbell, L.S. and Henderson, P. (1997) Apatite paragenesis in the Bayan Obo REE-Nb-Fe ore deposit, Inner Mongolia, China. Lithos, 42, 89–103.

Fialin, M. and Chopin, C. (2006) Electron-beam damage in triplite-group phosphates: Consequences for electron-microprobe analysis of fluorine. American Mineralogist, 91, 503–510.

Filiberto, J. and Treiman, A.H. (2009) The effect of chlorine on the liquidus of basalt: First results and implications for basalt genesis on Mars and Earth. Chemical Geology, 263, 60–68.

Fleet, M.E., Liu, X., and King, P.L. (2004) Accommodation of the carbonate ion in apatite: An FTIR and X-ray structure study of crystals synthesized at 2–4 GPa. American Mineralogist, 89, 1422–1432.

Gleadow, A.G.W., Belton, D.X., Kohn, B.P., and Brown, R.W. (2002) Fission track dating of phosphate minerals and the thermochronology of apatite. In M.J. Kohn, J. Rakovan, and J.M. Hughes, Eds., Phosphates—Geochemical, Geobiological, and Materials Importance, 48, p. 579–630. Reviews in Mineralogy and Geochemistry, Mineralogical Society of America, Chantilly, Virginia.

Hansen, E.C. and Harlov, D.E. (2007) Whole-rock, phosphate, and silicate compositional trends across amphibolite- to granulite-facies transition, Tamil Nadu, India. Journal of Petrology, 48, 1641–1680.

Harlov, D.E. and Förster, H.-J. (2002) High-grade fluid metasomatism on both a local and regional scale: the Seward Peninsula, Alaska and the Val Strona di Omegna, Ivrea-Verbano Zone, northern Italy. Part II: Phosphate mineral chemistry. Journal of Petrology, 43, 801–824.

——— (2003) Fluid-induced nucleation of (Y+REE)-phosphate minerals within

apatite: Nature and experiment. Part II. Fluorapatite. American Mineralogist, 88, 1209–1229.
Jarosewich, E., Nelen, J.A., and Norberg, J.A. (1980) Reference samples for electron microprobe analysis. Geostandards Newsletter, 4, 43–47.
Kerrick, D.M., Eminhizer, L.B., and Villaume, J.F. (1973) The role of carbon film thickness in electron microprobe analysis. American Mineralogist, 58, 920–925.
Klemme, S. and Dalpé, C. (2003) Trace-element partitioning between apatite and carbonatite melt. American Mineralogist, 88, 639–646.
Konzett, J., Rhede, D., and Frost, D.J. (2012) The high-PT stability of apatite and Cl partitioning between apatite and hydrous potassic phases in peridotite: An experimental study to 19 GPa with implications for the transport of P, Cl and K in the upper mantle. Contributions to Mineralogy and Petrology, 163, 277–296, DOI: 10.1007/s00410-011-0672-x.
Mathez, E.A. and Webster, J.D. (2005) Partitioning behavior of chlorine and fluorine in the system apatite-silicate melt-fluid. Geochimica et Cosmochimica Acta, 69, 1275–1286.
McCubbin, F.M. and Nekvasil, H. (2008) Maskelynite-hosted apatite in the Chassigny meteorite: Insights into late-stage magmatic volatile evolution in martian magmas. American Mineralogist, 93, 676–684.
McCubbin, F.M., Steele, A., Nekvasil, H., Schnieders, A., Rose, T., Fries, M., Carpenter, P.K., and Jolliff, B.L. (2010) Detection of structurally bound hydroxyl in fluorapatite from Apollo Mare basalt 15058,128 using TOF-SIMS. American Mineralogist, 95, 1141–1150.
McCubbin, F.M., Jolliff, B.L., Nekvasil, H., Carpenter, P.K., Zeigler, R.A., Steele, A., Elardo, S.M., and Lindsley, D.H. (2011) Fluorine and chlorine abundances in lunar apatite: Implications for heterogeneous distributions of magmatic volatiles in the lunar interior. Geochimica et Cosmochimica Acta, 75, 5073–5093.
Morgan, G.B. and London, D. (2005) Effect of current density on the electron microprobe analysis of alkali aluminosilicate glasses. American Mineralogist, 90, 1131–1138.
Pan, Y. and Fleet, M. (2002) Compositions of apatite-group minerals: Substitution mechanisms and controlling factors. In M.J. Kohn, J. Rakovan, and J.M. Hughes, Eds., Phosphates—Geochemical, Geobiological, and Materials Importance, 48, p. 13–49. Reviews in Mineralogy and Geochemistry, Mineralogical Society of America, Chantilly, Virginia.
Parat, F., Holtz, F., and Streck, M.J. (2011) Sulfur-bearing magmatic accessory minerals. In H. Behrens and J.D. Webster, Eds., Sulfur in Magmas and Melts: Its Importance for Natural and Technical Processes, 73, p. 285–314. Reviews in Mineralogy and Geochemistry, Mineralogical Society of America, Chantilly, Virginia.
Patiño Douce, A.E. and Roden, M. (2006) Apatite as a probe of halogen and water fugacities in the terrestrial planets. Geochimica et Cosmochimica Acta, 70, 3173–3196.
Patiño Douce, A.E., Roden, M.F., Chaumba, J., Fleisher, C., and Yogodzinski, G. (2011) Compositional variability of terrestrial mantle apatites, thermodynamic modeling of apatite volatile contents, and the halogen and water budgets of planetary mantles. Chemical Geology, 288, 14–31.
Paul, T.A. and Fitzgerald, P.G. (1992) Transmission electron microscopic investigation of fission tracks in fluorapatite. American Mineralogist, 77, 336–344.
Piccoli, P.M. and Candela, P.A. (2002) Apatite in igneous systems. In M.J. Kohn, J. Rakovan, and J.M. Hughes, Eds., Phosphates—Geochemical, Geobiological, and Materials Importance, 48, p. 255–292. Reviews in Mineralogy and Geochemistry, Mineralogical Society of America, Chantilly, Virginia.
Pouchou, J.L. and Pichoir, F. (1984) A new model for quantitative X-ray microanalysis, Part 1: Application to the analysis of homogeneous samples. La Recherche Aérospatiale (English ed.), 3, 13–38.
Pyle, J.M., Spear, F.S., and Wark, D.A. (2002) Electron microprobe analysis of REE in apatite, monazite and xenotime: Protocols and pitfalls. In M.J. Kohn, J. Rakovan, and J.M. Hughes, Eds., Phosphates—Geochemical, Geobiological, and Materials Importance, 48, p. 337–362. Reviews in Mineralogy and Geochemistry, Mineralogical Society of America, Chantilly, Virginia.
Sautter, V., Jambon, A., and Boudouma, O. (2006) Cl-amphibole in the nakhlite MIL 03346: Evidence for sediment contamination in a Martian meteorite. Earth and Planetary Science Letters, 252, 45–55.
Schettler, G., Gottschalk, M., and Harlov, D.E. (2011) A new semi-micro wet-chemical method for apatite analysis and its application to the crystal chemistry of fluorapatite-chlorapatite solid solutions. American Mineralogist, 96, 138–152.
Stormer, J.C. and Pierson, M.L (1993) Variation of F and Cl X-ray intensity due to anisotropic diffusion in apatite during electron microprobe analysis: an addendum. American Mineralogist Supplemental Data, http://www.minsocam.org/MSA/AmMin/Supplemental_Data/Stormer.html or http://www.webcitation.org/66Nh5qb5D.
Stormer, J.C., Pierson, M.L., and Tacker, R.C. (1993) Variation of F and Cl X-ray intensity due to anisotropic diffusion in apatite during electron microprobe analysis. American Mineralogist, 78, 641–648.
Streck, M.J. and Dilles, J.H. (1998) Sulfur evolution of oxidized arc magmas as recorded in apatite from a porphyry copper batholith. Geology, 26, 523–526.
Treiman, A.H., Barrett, R.A., and Gooding, J.L. (1993) Preterrestrial aqueous alteration of the Lafayette (SNC) meteorite. Meteoritics, 28, 86–97.
Webster, J.D., Tappen, C., and Mandeville, C.W. (2009) Partitioning behavior of chlorine and fluorine in the system apatite-melt-fluid. II: Felsic silicate systems at 200 MPa. Geochimica et Cosmochimica Acta, 73, 559–581.

Manuscript received February 21, 2011
Manuscript accepted March 19, 2012
Manuscript handled by George Morgan